K-edge x-ray-absorption spectroscopy of laser-generated Kr^+ and Kr^{2+}

S. H. Southworth, D. A. Arms, E. M. Dufresne, R. W. Dunford, D. L. Ederer,* C. Höhr,† E. P. Kanter, B. Krässig, E. C. Landahl, E. R. Peterson,‡ J. Rudati,§ R. Santra, D. A. Walko, and L. Young
Argonne National Laboratory, Argonne, Illinois 60439, USA
(Received 1 August 2007; published 24 October 2007)

Tunable, polarized, microfocused x-ray pulses were used to record x-ray absorption spectra across the *K* edges of Kr^+ and Kr^{2+} produced by laser ionization of Kr. Prominent $1s \rightarrow 4p$ and $5p$ excitations are observed below the $1s$ ionization thresholds in accord with calculated transition energies and probabilities. Due to alignment of $4p$ hole states in the laser-ionization process, the Kr^+ $1s \rightarrow 4p$ cross section varies with respect to the angle between the laser and x-ray polarization vectors. This effect is used to determine the Kr^+ $4p_{3/2}$ and $4p_{1/2}$ quantum state populations, and these are compared with results of an adiabatic strong-field ionization theory that includes spin-orbit coupling.

DOI: 10.1103/PhysRevA.76.043421 PACS number(s): 32.80.Rm, 32.80.Hd, 32.30.Rj

I. INTRODUCTION

The strong electric fields produced by focused pulses of ultrafast optical lasers interact with atoms nonperturbatively and can remove an outer-shell electron by multiphoton or tunnel ionization [1,2]. Additional electrons can be removed by the same laser pulse in a sequential ionization process or the oscillating field can drive the photoelectron back to the incipient ion and produce multiple ionization or high-order harmonic radiation [2]. Strong-field laser-atom interactions underlie current efforts to push high-order harmonic generation into the soft x-ray regime [3] and to generate and utilize attosecond light pulses [4]. Theoretical models of laser ionization and high-order harmonic generation are usually tested by comparison with measurements of ion charge-state yields, photoelectron spectra, or high-order harmonic radiation [2,3]. We have developed a spectroscopic probe of atoms and molecules in intense laser fields that uses tunable, polarized, microfocused x-ray pulses to record x-ray absorption spectra [5–7]. Notable advantages of x rays include atomic specificity, high penetration through dense targets, and ultrafast response to x-ray absorption by emission of x-ray fluorescence or Auger electrons. The methods are similar to other applications of time-resolved x-ray absorption spectroscopy, for example, to studies of laser ionization [8], transient molecular structures [9], and solvation dynamics [10]. The laser-pump–x-ray-microprobe technique provides spectral tunability, variable laser polarization with linearly polarized x rays, pump-probe delays from picoseconds to milliseconds, and ~ 10 μm x-ray spatial resolution. Both isolated atomic properties and the collective response of macroscopic systems can be investigated. In an earlier experiment, orbital alignment of Kr^+ $4p$ hole states produced by laser ionization was observed from the dependence of the $1s \rightarrow 4p$ resonant x-ray absorption cross section on the angle between the laser and x-ray polarization vectors [6]. Theoretical analysis of the experiment demonstrated that it is essential to include spin-orbit coupling in models of strong-field ionization of Kr [11]. The polarization dependence of the $1s \rightarrow 4p$ resonance and the variable pump-probe delay were also used to follow the time evolution of the collective Kr^+ alignment in the e^--Kr^+ plasma produced by laser ionization [7]. That paper presented a theoretical model that accounts for the time-dependent dealignment and also reported on the effects of imposing an external magnetic field.

Both experiments [6,7] used the $1s \rightarrow 4p$ resonance of Kr^+. The present paper gives a detailed analysis of x-ray absorption spectra across the *K* edges of Kr^+ and Kr^{2+}. The data were fit to model spectra generated by combining discrete transitions from the relativistic configuration-interaction calculations of Ref. [12] with continua that are taken to be the same as that of neutral Kr after accounting for the ionization threshold shifts [13]. Prominent $1s \rightarrow 4p$ and $5p$ transitions distinguish the absorption spectra of Kr^+ and Kr^{2+} from that of Kr. We note that while our experiments were motivated by interest in developing a tunable x-ray microprobe of atoms and molecules in strong laser fields, the methods also provide an approach to recording x-ray absorption spectra of ions that are of general interest in studies of laboratory and astrophysical plasmas [14].

We also compare x-ray absorption spectra of Kr^+ produced by circularly polarized laser light and linearly polarized laser light with the polarization parallel and perpendicular to the x-ray polarization. The $1s \rightarrow 4p$ cross section varies with polarization due to alignment of Kr^+ $4p$ hole states [6]. This effect is used to determine $\rho_{3/2,3/2}$, $\rho_{3/2,1/2}$, and $\rho_{1/2,1/2}$, where $\rho_{j,|m_j|}$ is the probability of producing a hole in the $4p_{j,\pm m_j}$ states. These are compared with results of an adiabatic strong-field ionization theory that includes spin-orbit coupling [11]. A similar experiment and theoretical calculation were recently reported in which extreme ultraviolet high-order harmonic radiation was used to probe quantum state populations of Xe^+ produced by laser ionization [15]. Comparison of theory and experiment for the Kr and Xe cases yields new insight into strong-field ionization.

*Present address: Tulane University, New Orleans, Louisiana 70118, USA.
†Present address: TRIUMF, Vancouver, British Columbia, Canada V6T 2A3.
‡Present address: University of Michigan, Ann Arbor, Michigan 48109, USA.
§Present address: Xradia Inc., Concord, California 94520, USA.

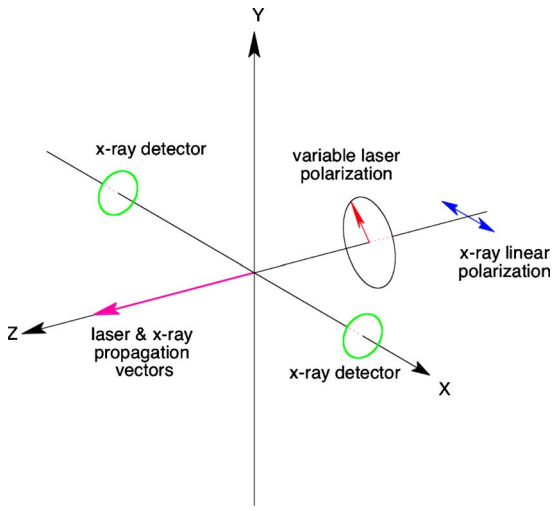

FIG. 1. (Color online) The geometry used to record x-ray absorption spectra of laser-generated Kr^+ and Kr^{2+}. The z axis is taken along the collinear propagation directions of the laser and x-ray beams. The laser produces ions within a focal volume centered at the origin. X-ray pulses arrive ≤ 1 ns after the laser pulses. X rays absorbed by ions or neutrals produce K vacancies that relax by emitting x-ray fluorescence. The emitted x rays are detected over small solid angles around the x axis. The x-ray beam is linearly polarized along the x axis. The laser beam is circularly polarized or linearly polarized with polarization parallel or perpendicular to the x-ray polarization.

Section II of this paper describes the x-ray microprobe technique. Section III compares measured x-ray absorption spectra of Kr, Kr^+, and Kr^{2+} and model spectra generated from the calculations of Ref. [12]. Quantum state populations of Kr^+ are then determined from polarization-dependent $1s \rightarrow 4p$ cross sections and compared with the calculations of Ref. [11]. Conclusions and suggestions for future research and applications are in Sec. IV.

II. EXPERIMENTAL METHODS

The experiments were performed at beamline 7-ID of Argonne's Advanced Photon Source (APS) in combination with a Ti:sapphire ultrafast laser system that is phase-locked to the radio-frequency (RF) clock of the storage ring. Detailed descriptions of the laser system and its synchronization with the x-ray pulses are given in Refs. [5,16]. Two sets of measurements were made with different gas targets, laser intensities and polarizations, and beamline monochromators. The geometry of beams and detectors shown in Fig. 1 was common to all experiments.

The first experiments used a gas jet of Kr in a high-vacuum chamber. The linearly polarized laser beam passed through a quarter-wave plate to produce circularly polarized light in 1.3 mJ, 50 fs, 1 kHz pulses at a central wavelength of 800 nm. The unfocused beam entered an optical window at the rear of the chamber traveling opposite the direction and slightly shifted from the x-ray beam. A tiltable spherical mirror near the front of the chamber reflected the laser beam back along the direction of the x rays and focused it within the Kr jet to ~ 100 μm full-width-at-half-maximum (FWHM) diameter with a Rayleigh range ~ 30 mm. The estimated peak intensity of 4×10^{14} W/cm^2 exceeded the saturation intensity for ionization of a Kr $4p$ electron using 800 nm light [17,18]. With a density of $\sim 10^{13}$ Kr atoms/cm^3, the laser produced $\sim 10^7$ ions/pulse. An isolated aperture plate located near the gas jet was biased to -5 V and connected to a current amplifier to measure the ion current. The diverging laser beam exited the target chamber through the rear optical window and was refocused into a power meter.

The laser produced a long, narrow cylinder of ions to be probed by the x rays. A pair of 20-cm-long bendable mirrors in Kirkpatrick-Baez (KB) geometry were positioned just upstream of the target chamber to focus the x-ray beam [19]. The mirrors accepted and focused $\sim 40\%$ of the incident x-ray flux to ≤ 10 μm FWHM diameter within the gas jet. The x rays entered the chamber through a beryllium window and passed through a 1-mm hole in the center of the laser-focusing mirror. The mirror also served to block x rays scattered from the beryllium window. The x rays exited the chamber through a hole sealed with Kapton tape at the center of the optical window. The x rays then passed through an ionization chamber to measure their flux and hit a fast photodiode to determine their time of arrival. A portion of the laser beam that exited the chamber could also hit the photodiode and produce a timing signal. With copropagating laser and x-ray beams, the time delay between laser and x-ray pulses was directly measured with the photodiode and a fast oscilloscope. The photodiode has a rise time ~ 1 ns, which was sufficient for setting an initial x-ray pulse delay of a few ns after the laser pulse. Precise timing was determined by cross correlation scans described below.

The KB mirrors were tilted and bent to give the smallest focal spot with maximum intensity. The angles of incidence on the mirrors were 4 mrad to efficiently reflect x rays near the Kr K edge of 14.3 keV, so the focused x-ray beam was deflected by 8 mrad horizontally and vertically. The chamber was centered along the deflected x-ray beam path, and a scintillator screen (YAG or BGO) was moved into the gas jet position to view the laser and x-ray focal spots with a CCD camera and imaging software. The angular positions of the laser focusing mirror were adjusted to move the focal spot to within ~ 100 μm of the x-ray spot by viewing their positions on the scintillator. For precise overlap, a knife edge was scanned with ~ 1 μm steps through the laser and x-ray beams. The intensities of the laser and x-ray beams were measured downstream while the knife edge was scanned vertically or horizontally. The laser power was reduced to $<1\%$ to avoid ablating the knife edge. Neutral density filters were problematic for this purpose because they shifted the beam path. Metallic-coated pellicle beamsplitters worked well to reduce beam intensity with negligible beam motion, but care was needed to avoid pellicle heating and damage that could distort the wavefront. Using knife-edge scans, the angular position of the laser-focus mirror was adjusted to overlap the laser and x-ray focal spots within the gas jet. The crossing angle between the beams was ~ 25 mrad, so they overlapped over ~ 4 mm of beam path.

For the first experiment, a single silicon-drift x-ray detector was positioned at 90° to the beams along the x-ray po-

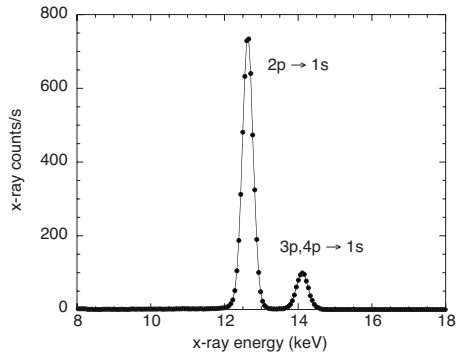

FIG. 2. *K* x-ray fluorescence spectrum of Kr recorded with a silicon-drift detector following absorption of 14.360 keV x rays. Relative absorption spectra across the *K* edges of Kr, Kr^+, and Kr^{2+} were determined from the $2p \rightarrow 1s$ count rates.

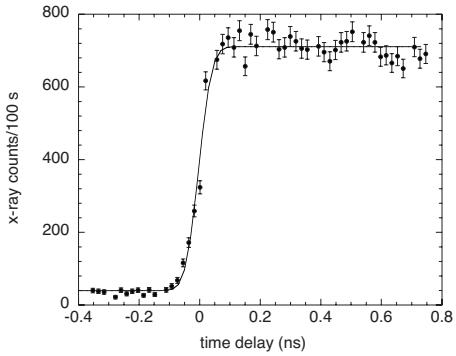

FIG. 3. Cross correlation scan obtained by measuring x-ray fluorescence counts excited at the Kr^+ $1s \rightarrow 4p$ resonance vs. time delay between laser and x-ray pulses. The fitted curve is a Gauss error function with 98 ± 5 ps FWHM.

larization direction to record x-ray fluorescence. Two detectors were used in later experiments as indicated in Fig. 1. A molybdenum aperture selected fluorescence from ~2 mm of beam path centered on the overlap region. The detector resolution was sufficient to resolve the $2p \rightarrow 1s$ ($K\alpha$) fluorescence from $3p,4p \rightarrow 1s$ ($K\beta$) transitions as shown in Fig. 2. Differences in the fluorescence energies of Kr, Kr^+, and Kr^{2+} are small compared with the ~200 eV resolution of the detector. A single channel analyzer (SCA) selected counts in the $K\alpha$ peaks as the absorbed photon energy was scanned across the *K* edges. The SCA excluded x rays due to beam scatter or fluorescence from metallic surfaces. Combining the total fluorescence yield for a Kr *K* vacancy [20] with calculated *K* x-ray emission rates [21], the probability for a Kr *K* vacancy to decay by a $2p \rightarrow 1s$ transition is estimated to be 0.54. We assume that this probability is independent of the absorbed photon energy and is the same for Kr, Kr^+, and Kr^{2+}. The numbers of $K\alpha$ x rays counted are then proportional to the *K*-shell photoabsorption cross sections. Since $K\alpha$ fluorescence is produced only by excitation or ionization of a 1*s* electron, the relative absorption cross sections excluded absorption by electrons in higher shells.

The storage ring was operated in top-up mode in which the electron current is maintained at 100 mA. This gives a constant power load on beamline optics that enhances stabilities of x-ray beam position and flux. The undulator produced x rays in its third harmonic near the 14.3 keV *K* edge of Kr with a bandwidth ~100 eV. The first experiments used a fixed-offset, cryogenically cooled, double-crystal monochromator [22] with Si(111) crystals that selected a narrow band of x rays from the undulator. The bandwidth was determined by measuring the rocking curve of a high-resolution crystal reflection [23]. A Si(440) channel-cut crystal was used to measure a bandwidth of 1.5 eV FWHM, and an ionization chamber measured the x-ray beam flux $\sim 10^{13}$ s^{-1}.

The storage ring's RF system runs at 352 MHz and a harmonic number of 1296. The revolution time for a single electron bunch is 3.682 μs. The storage ring was operated in hybrid-singlet mode in which a single electron bunch containing 8–16 mA was isolated by 1.59 μs gaps from 56 bunches containing the remainder of the 100 mA current. The singlet provides ~100 ps FWHM x-ray pulses at 272 kHz that are well suited for time-resolved measurements. The silicon drift detectors have timing resolutions ~0.5 μs FWHM, which is fast enough that electronic gates could be used to select fluorescence produced only by the singlets. Timing gates selected fluorescence signals produced by all of the singlets at 272 kHz and by the particular singlets synchronized with the 1 kHz laser pulses. A small fraction of the x-ray flux of the beamline was usable as probe pulses, primarily due to the mismatch in repetition rates of the laser and storage ring, with additional losses from the acceptance and reflectivity of the KB mirrors. Nevertheless, a flux of $\sim 10^6$ x rays per pulse was obtained with 1.5 eV bandwidth and ~10 μm focal diameter.

Laser ionization makes a 4*p* hole that can be filled in a $1s \rightarrow 4p$ transition that produces a prominent resonant feature at 14313 eV in the photoabsorption spectrum of Kr^+. The resonance is below the onset of strong absorption in Kr so it gives good contrast of fluorescence from Kr^+ compared with Kr. The laser-on–laser-off fluorescence ratio can be large (10–50) on resonance and is sensitive to the laser–x-ray overlap within the detector's viewing region. This effect was used to optimize the overlap after the knife-edge scans.

The precise time delay between the ~50 fs laser pulses and ~100 ps x-ray pulses was determined by cross correlation scans of the x-ray fluorescence counts excited at the Kr^+ $1s \rightarrow 4p$ resonance. Note that x-ray absorption and fluorescence is a subfemtosecond process and that the gas-phase target is continually replenished. The timing delay was controlled to 19 ps steps by a digital phase shifter in the RF reference from the storage ring and digital delay of the laser Pockels' cell trigger [16], and the jitter was measured to be ~3 ps [5]. A fit to the rising edge of the delay scan in Fig. 3 gives 98 ± 5 ps FWHM for x-ray pulses produced by singlets containing 8 mA of stored current. In Ref. [7], the time evolution of the e^--Kr^+ plasma was studied by extending delay scans to 30 ns. For measurements of x-ray absorption spectra, the delay was set to ≤ 1 ns. The plateau in the fluorescence count rate in Fig. 3 indicates that the ion density is unaffected by Coulomb expansion below ~1 ns.

The focused x-ray beam must maintain a stable position through the laser focal volume while scanning the undulator and beamline monochromator by ~75 eV across the *K*

edges. Significant motion of the x-ray focus was initially observed while scanning the monochromator. Stable positioning was achieved using a proportional-integral-derivative (PID) control routine to adjust the monochromator's second-crystal angle with a piezoelectric tilter to maintain a constant position signal from an x-ray beam-position monitor [24,25]. Scintillator images and knife-edge scans of the x-ray focal spot indicated ~ 1 μm stability.

In the course of this research, the beamline monochromator was replaced by a Kohzu HLD-4 double-crystal monochromator using diamond(111) crystals. The resolution measured at 9887 eV with a Si(555) back reflection implies a bandwidth of 0.8 eV FWHM at the Kr K edge. This is smaller than the 1.5 eV resolution of the Si(111) monochromator, due to the narrower Darwin width of diamond, and the reflected x-ray flux is correspondingly smaller [23]. The widths of photoabsorption lines measured with both monochromators are dominated by the 2.7 eV lifetime width of Kr K vacancies [26].

A flowing-gas cell was used in the second set of experiments to measure x-ray absorption spectra of Kr^+ with the diamond monochromator. The gas cell apparatus accommodates higher Kr densities and the application of an external magnetic field for studies of alignment [7]. The laser beam was focused by an external lens and entered the front of the gas cell through an optical window. X rays from the KB mirrors entered a hole in the window sealed with Kapton tape. The two beams exited the gas cell through a similar window and their intensities were measured. An x-ray scintillator and knife-edge scans were used for the focusing and spatial overlap procedures. The position of the laser focusing lens was adjusted to precisely overlap the laser and x-ray focal volumes, and the initial timing overlap was done with a fast photodiode. Fluorescent x rays from the overlap region were selected with apertures, exited the gas cell through Kapton windows, and were recorded by two silicon-drift detectors positioned as indicated in Fig. 1. The overlap was optimized by maximizing fluorescence excited at the Kr^+ $1s \rightarrow 4p$ resonance with the time delay set to ≤ 1 ns. The linearly polarized laser beam passed through a half-wave plate, upstream of the focusing lens, to set the laser polarization either parallel or perpendicular to the x-ray polarization. Alternatively, a quarter-wave plate was used to produce circularly polarized laser light.

III. RESULTS AND DISCUSSION

The K-edge photoabsorption spectra of Kr, Kr^+, and Kr^{2+} measured with the Si(111) beamline monochromator are compared in Fig. 4. The laser-off spectrum is for neutral Kr, while the laser-on data show the spectra of Kr^+ and Kr^{2+} generated by circularly polarized laser light. The Kr contribution to the laser-on data has been subtracted. A fit gave weights of 0.44, 0.41, and 0.14 for the Kr, Kr^+, and Kr^{2+} components, respectively. The spectra consist of discrete and continuum components broadened by 2.7 eV lifetime widths and 1.5 eV instrumental widths. The $1s \rightarrow np$ $(n \geq 5)$ and continuum components of the Kr spectrum blend into a nearly featureless edge with an inflection point at 14323.5 eV [27]. Laser ionization removes one or two $4p$ electrons, and prominent $1s \rightarrow 4p$ transitions appear in the ions' absorption spectra. Distinct $1s \rightarrow 5p$ transitions are also observed as a result of the increased spacings among Rydberg states and continua. These features distinguish the ions' spectra from that of Kr.

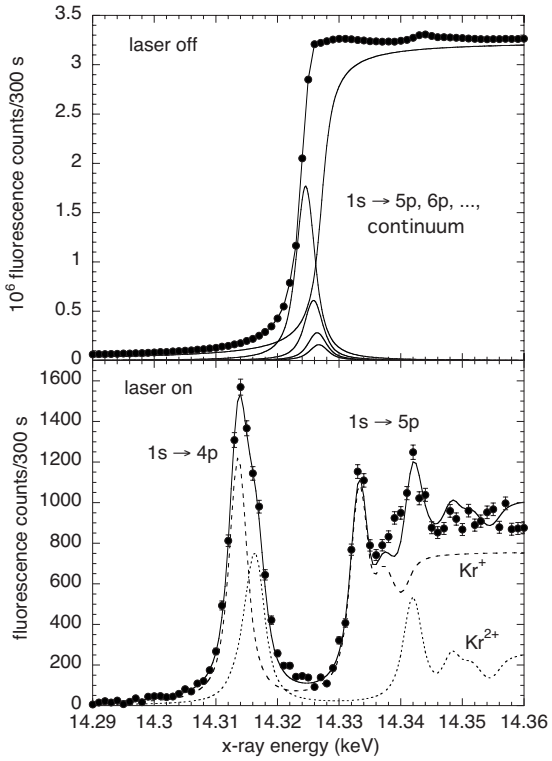

FIG. 4. K-edge photoabsorption spectra of Kr, Kr^+, and Kr^{2+} determined from x-ray fluorescence counting rates. Top: laser-off spectrum of Kr (circles with connecting line) along with $1s \rightarrow np$ $(n \geq 5)$ and continuum components suggested by the fitted spectrum in Ref. [27]. Bottom: laser-on spectrum (circles) with fits to Kr^+ (dashed curve) and Kr^{2+} (dotted curve) components. The solid curve is the sum of the two fitted components. The ions were generated by circularly polarized laser light, and the residual Kr component has been subtracted.

The curves fit to the discrete transitions in the Kr^+ and Kr^{2+} spectra are based on the $1s \rightarrow np$ $(n=4-8)$ transition energies and probabilities calculated by Pan *et al.* [12]. The calculations include relativistic, QED, relaxation, and correlation effects and energy shifts due to discrete states interacting with continua. Comparisons of the calculated transition energies with available experimental data are discussed in Ref. [12]. For example, the measured Kr $1s$ ionization energy determined by analysis of the K-edge absorption spectrum [27] agrees with measurements based on x-ray fluorescence and photoelectron spectroscopy [28,29] and provides an experimental reference energy of 14327.19 (13) eV [28]. The Kr $4p_{3/2}$ and $4p_{1/2}$ ionization energies are 14.000 and 14.665 eV, respectively [30]. Subtracting those energies from the $1s$ ionization energy gives the positions of the Kr^+ $1s \rightarrow 4p_{3/2}$ and $4p_{1/2}$ resonances at 14313.19 (13) eV and 14312.53 (13) eV. The calculated transition energies are ~ 1 eV higher at 14314.127 eV and 14313.461 eV. The

agreement between experimental and calculated energies is excellent considering the large transition energies, and the ~1 eV deviations are smaller than the 2.7 eV lifetime width.

The calculated transition energies and probabilities [12] were used to generate the discrete parts of model spectra of Kr^+ and Kr^{2+} that were fit to the laser-on spectrum. The Kr^+ initial states are $4p^5\ ^2P_{1/2}$ and $^2P_{3/2}$ and the Kr^{2+} initial states are $4p^4\ ^3P_0$, $^1S_0$, $^3P_1$, $^3P_2$, and $^1D_2$. We assumed that the relative populations of the initial states were statistical and that the magnetic sublevels were equally populated. These assumptions ignore nonstatistical branching ratios and alignment of hole states that result from the laser ionization process [11]. Those effects were included in the analysis of a second set of Kr^+ absorption spectra discussed later.

To generate the continuum parts of the model spectra, we note that, for example, Reilman and Manson [13] calculated the $1s$ photoionization cross sections of Fe^{q+} ($q=0-23$) and found that the cross sections agree with that of neutral Fe within ~2%. The cross sections are truncated on the low-energy side as the $1s$ ionization energy increases with charge state. Following that model, the $1s$ continua of Kr^+ and Kr^{2+} are expected to be the same as that of Kr after accounting for the increased ionization thresholds.

The calculated transition probabilities of Ref. [12] are spontaneous emission probabilities A_{ki}, where k and i represent the upper and lower levels, respectively. For comparison with x-ray absorption spectra, the A_{ki} values can be converted to absorption oscillator strengths f_{ik} by [31]

$$f_{ik} = \frac{mc\epsilon_0\lambda^2}{2\pi e^2}\frac{g_k}{g_i}A_{ki}, \tag{1}$$

where m and e are the electron mass and charge, c is the speed of light, ϵ_0 is the permittivity of free space, λ is the transition wavelength, and g_k and g_i are the degeneracies of the upper and lower levels. The oscillator strength for a discrete transition is expressed as an absorption cross section by [32]

$$\sigma(\omega) = \frac{2\pi^2 e^2}{mc}f_{ik}. \tag{2}$$

In the continuum region, f_{ik} is replaced by the differential oscillator strength df/dE [32]. The calculated discrete cross sections were convolved with 2.7 eV Lorentzians to account for lifetime broadening and 1.5 eV Gaussians to account for the instrumental bandwidth. For the continua we used a cross section of 14.7 kb [33], with thresholds of 14340.4 eV for Kr^+ and 14355.5 eV for Kr^{2+}, which are ~1 eV below the calculated edge energies of Ref. [12]. To account for the 2.7 eV lifetime broadening, the continuum edges were given arctangent shapes as described in Ref. [34]. The laser-on spectrum in Fig. 4 was then fit to the two model spectra. Prominent $1s\rightarrow 4p$ and $5p$ transitions are evident in the absorption spectra of both ions. In comparison with the Kr spectrum, the spectra of the ions show increased oscillator strengths in the discrete transitions due to the open $4p$ shells and loss of continuum cross section due to the higher $1s$ ionization energies.

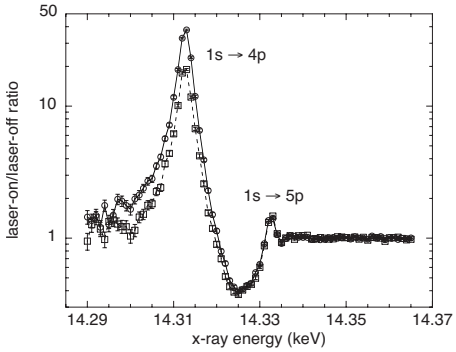

FIG. 5. Ratios of x-ray fluorescence counts measured with laser on to laser off vs absorbed x-ray energy. Data are plotted for laser polarization parallel (circles connected with solid curve) and perpendicular (squares connected with dashed curve) to the x-ray polarization. Peaks are observed at the Kr^+ $1s\rightarrow 4p$ and $5p$ resonances.

In a subsequent experiment, linearly polarized laser light generated Kr^+ in the gas cell, and x-ray absorption spectra were recorded using the beamline's diamond monochromator. A half-wave plate oriented the laser polarization either parallel or perpendicular to the polarization of the x rays. The undulator and monochromator energies were scanned together, and fluorescent x rays were counted with laser on and off for parallel and perpendicular polarizations. Results for the laser-on–laser-off ratios of fluorescence counts are plotted in Fig. 5. The on-off ratio is determined by the relative absorption cross sections of neutrals and ions and the numbers of neutrals and ions observed by the fluorescence detectors. The ion density was apparently unaffected by Coulomb expansion with $\leq$1 ns time delay between laser and x-ray pulses (see Fig. 3 and Ref. [7]). The ratio is large near the Kr^+ $1s\rightarrow 4p$ resonance where the neutral cross section is small. The ratio passes through a minimum near 14.325 keV where the neutral cross section is rising while the Kr^+ cross section is small between the $4p$ and $5p$ resonances. A small maximum appears at the $5p$ resonance, and the ratio $\approx$1 above 14.336 keV. This confirms the expectation that the continuum cross sections of Kr and Kr^+ are nearly equal. In the limit of 100% conversion of Kr to Kr^+, the relative cross sections indicate that the ratio with parallel polarization can be as large as 54 on the $4p$ resonance and as small as 0.15 at 14.325 keV.

The laser-on–laser-off ratio for parallel polarization is about twice as large as for perpendicular polarization at the Kr^+ $4p$ resonance, so the absorption cross sections differ by a factor ~2. This is shown in the relative cross sections determined from the same data and plotted in Fig. 6. A single normalization factor was used to scale the parallel and perpendicular results to 1 at high energy. A spectrum for Kr^+ generated by circularly polarized laser light was also recorded and scaled to 1 at high energy. The data were fit to Kr, Kr^+, and Kr^{2+} components in a procedure similar to that used for the data in Fig. 4. However, the ~0.8 eV bandwidth of the diamond monochromator was not included in the fits, since it had negligible effect compared with the 2.7 eV lifetime broadening. The fits gave Kr components of ~30% in

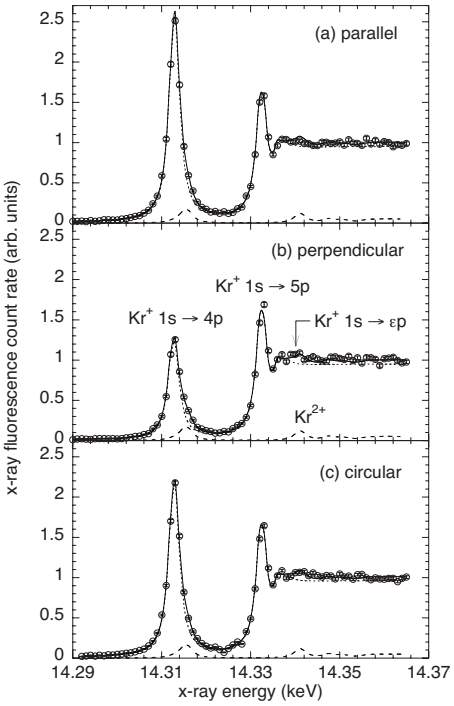

FIG. 6. *K*-edge photoabsorption spectra of ions produced with different laser polarizations. The circles are the measured x-ray fluorescence counting rates with the neutral Kr contributions removed. The dotted curves are fits to the Kr^+ components, the dashed curves are fits to the Kr^{2+} components, and the solid curves are the total fits. (a) Ions generated by linearly polarized laser light with polarization parallel to that of the x-ray beam. (b) Ions generated by linearly polarized laser light with polarization perpendicular to that of the x-ray beam. (c) Ions generated by circularly polarized laser light.

the two linearly polarized spectra and ~50% in the circularly polarized spectrum. Although the $1s \rightarrow 4p$ resonances of Kr^+ and Kr^{2+} are overlapped, the $1s \rightarrow 5p$ resonance of Kr^{2+} makes a distinct feature, as shown in the earlier data of Fig. 4. This feature was used to discern small Kr^{2+} components of ~3% in fits to the data of Fig. 6. The fitted Kr^+ components show qualitatively how the spectrum varies with laser polarization. Relative to the continuum cross sections above ~14.34 keV, the $1s \rightarrow 5p$ cross sections are about the same, while the $1s \rightarrow 4p$ cross sections vary by a factor ~2. This is due to alignment of laser-generated Kr^+ $4p$ hole states as shown in Ref. [6] and calculated in Ref. [11]. Both the nonrelativistic tunnel ionization model and nonrelativistic multiphoton ionization model predict a strong propensity for removing a $4p$, $m_l=0$ electron, where the quantization axis is taken along the linear polarization direction of the laser field. A dependence of the $1s \rightarrow 4p$ cross section on the angle between the linear polarization vectors of the laser and x rays is expected and observed, but the measured parallel-to-perpendicular cross section ratio (≈ 2) is much smaller than predicted by the nonrelativistic models. Inclusion of spin-orbit coupling leads to calculated cross section ratios close to the measured ratio [11]. These results highlight the roles of orbital alignment and spin-orbit coupling in the laser ionization process. For circularly polarized laser light, the nonrelativistic models suggest that $4p$ electrons are removed symmetrically about the propagation direction in a donut pattern. The measured $1s \rightarrow 4p$ cross section is between those measured with the two linear polarizations.

A further experimental test of laser ionization theory [11] is given by determining Kr^+ quantum state populations from fitting the parallel and perpendicular cross sections in Fig. 6 to $1s \rightarrow 4p_{3/2}$ and $4p_{1/2}$ components. In the following, linearly polarized laser radiation is assumed, and the laser polarization axis is chosen as the quantization axis. Let $|4p_j,m\rangle \equiv |j,m\rangle$ denote the eigenstate of Kr^+ with a hole in the $4p_j$ orbital with projection quantum number m, and let $\rho_j^{(m)}$ be the probability of finding Kr^+ in this state. The probabilities are normalized such that $\Sigma_{j,m}\rho_j^{(m)}=1$. Krypton ions with a hole in the $4p$ shell have a spin-orbit period of $T^{(\mathrm{SO})}=6.2$ fs, corresponding to the 0.665 eV fine-structure splitting between the $|4p_{3/2},m\rangle$ and $|4p_{1/2},m\rangle$ states. Since in our experiment, both laser and x-ray pulses are long in comparison to $T^{(\mathrm{SO})}$, any coherences in the density matrix of Kr^+ remain unobserved [11]. Under these circumstances, the x-ray absorption signal depends only on the diagonal elements $\rho_j^{(m)}$ of the ion density matrix. The x-ray absorption cross section in the vicinity of the $1s \rightarrow 4p$ resonance of Kr^+ is thus obtained by the usual procedure of averaging over the initial states of the ion and summing over the final states

$$\sigma(\omega_x,\vartheta_x) = \sum_{j,m} \rho_j^{(m)} \frac{2\pi\alpha\omega_x\Gamma_K}{(E_K - E_j - \omega_x)^2 + \Gamma_K^2/4} \times \sum_{m'} |\langle j,m|\boldsymbol{d}\cdot\boldsymbol{\epsilon}_x|K,m'\rangle|^2. \quad (3)$$

In this expression (written in atomic units), α is the fine-structure constant, ω_x is the x-ray photon energy, E_K and Γ_K are the energy and decay width, respectively, of the state $|K,m'\rangle$ with a hole in the K shell (filled valence shell), and E_j is the energy of the state $|j,m\rangle$. The parameter ϑ_x stands for the angle between the x-ray polarization vector $\boldsymbol{\epsilon}_x$ and the quantization axis, and $\boldsymbol{d}$ is the electric dipole operator in length form.

The x-ray absorption cross section of an unaligned ensemble of ions in the state $|j,m\rangle$ (fixed j, uniform population of m) is

$$\sigma_j(\omega_x) = \frac{2\pi\alpha\omega_x\Gamma_K}{(E_K - E_j - \omega_x)^2 + \Gamma_K^2/4} \frac{|\langle j||d||K\rangle|^2}{3(2j+1)}, \quad (4)$$

where $\langle j||d||K\rangle$ is a reduced matrix element [35]. Thus, with the help of the Wigner-Eckart theorem [35], Eq. (3) may be written as

$$\sigma(\omega_x,\vartheta_x) = 3\sum_j \sigma_j(\omega_x) \sum_m \rho_j^{(m)} \left\{ \cos^2(\vartheta_x) C^2\left(\frac{1}{2},1,j;m,0,m\right) + \frac{1}{2}\sin^2(\vartheta_x) C^2\left(\frac{1}{2},1,j;m+1,-1,m\right) + \frac{1}{2}\sin^2(\vartheta_x) C^2\left(\frac{1}{2},1,j;m-1,+1,m\right) \right\}. \quad (5)$$

Here, $C(j_1,j_2,j;m_1,m_2,m)$ is a Clebsch-Gordan coefficient [36]. It follows that

$$\sigma(\omega_x,0°) = 2\rho_{3/2,1/2}\sigma_{3/2}(\omega_x) + \rho_{1/2,1/2}\sigma_{1/2}(\omega_x) \tag{6}$$

and

$$\sigma(\omega_x,90°) = \frac{1}{2}\{\rho_{3/2,1/2} + 3\rho_{3/2,3/2}\}\sigma_{3/2}(\omega_x) + \rho_{1/2,1/2}\sigma_{1/2}(\omega_x), \tag{7}$$

where $\rho_{j,|m|} \equiv \rho_j^{(m)} + \rho_j^{(-m)}$ denotes the probability of finding Kr^+ with a hole in either the $4p_j,m$ or the $4p_j,-m$ orbital. Using Eqs. (6) and (7), it may be verified that if the $j=3/2$ state is not aligned ($\rho_{3/2,1/2}=\rho_{3/2,3/2}$), then $\sigma(\omega_x,0°) = \sigma(\omega_x,90°)$. The $j=1/2$ state does not display a polarization dependence.

The parallel and perpendicular spectra of Fig. 6 were fit simultaneously to six components consisting of neutrals, Kr^{2+}, and Kr^+ components for $1s\rightarrow 4p_{3/2}$, $1s\rightarrow 4p_{1/2}$, $1s\rightarrow np$ ($n=5-8$), and the $1s$ continuum. The fitting functions were generated as described earlier using the calculated transition probabilities and relative energies of Ref. [12] with 2.7 eV FWHM Lorentzian line shapes. Although the Kr^+ $1s\rightarrow 4p_{3/2}$ and $4p_{1/2}$ components are unresolved, their energy separation is fixed by the well-known spin-orbit splitting of 0.665 eV [30]. As noted earlier, the calculated transition energies are ~1 eV higher than the experimental energies. The fits retained the calculated relative energies, but an overall shift was allowed to best fit the measured spectra. Since only the $4p_{3/2}$ hole state can be aligned and only the $1s\rightarrow 4p_{3/2}$ transition varies significantly with polarization, the fits were constrained so that only the $1s\rightarrow 4p_{3/2}$ component varied between the two spectra. The data and fitted curves in the $1s\rightarrow 4p$ region are shown in Fig. 7. Additional broadening of the $1s\rightarrow 4p_{3/2}$ and $4p_{1/2}$ components with 0.8 eV FWHM Gaussians to account for the monochromator band pass had negligible effect on the fitted results. Combining the fitted intensities with Eqs. (6) and (7) gives the experimental quantum state populations in Table I. The uncertainties represent 2σ statistical errors from the fits. We examined the influence of various systematic uncertainties in the fits, by varying relative peak positions and including the monochromator band width, and all were small in comparison with the tabulated errors. Uncertainties in the calculated transition probabilities [12] are difficult to estimate and have been neglected in this analysis.

Reference [11] develops an adiabatic strong-field ionization theory that takes spin-orbit coupling explicitly into account. The method makes use of a flexible finite-element basis set and determines ionization rates in this square-integrable basis using a complex absorbing potential [37,38]. The method is thus applicable to both tunneling and over-the-barrier ionization problems. Rate equations are employed to follow the temporal evolution of the atomic state populations during the laser pulse. Using this theory, and defining the saturation intensity in accordance with Ref. [39], we calculate for Kr a saturation intensity of 1.6×10^{14} W/cm^2, in agreement with experiment [17,18]. Within the model, the peak intensity needed to obtain in the laser focus a 30% population of neutral atoms (after the laser pulse is over) is 1.9×10^{14} W/cm^2. At this intensity, which roughly matches the experimental conditions for the data in Figs. 6 and 7, the Kr^+ populations calculated utilizing the theory from Ref. [11] are $\rho_{3/2,1/2}=71\%$, $\rho_{1/2,1/2}=25\%$, and $\rho_{3/2,3/2}=4\%$. (The $\rho_{j,|m|}$ reported in Ref. [11] were obtained at 2.5×10^{14} W/cm^2.)

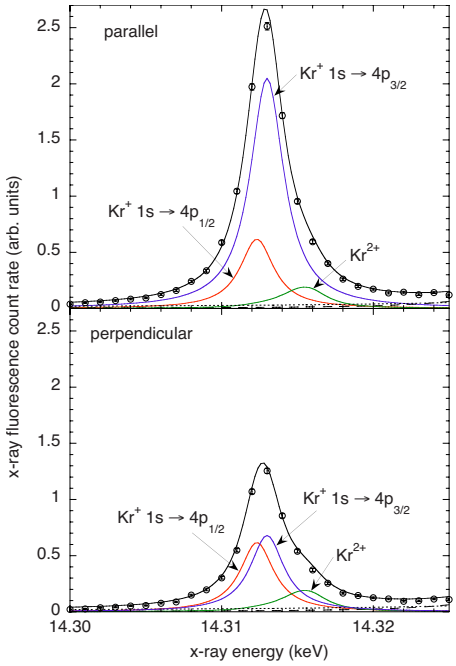

FIG. 7. (Color online) The $1s\rightarrow 4p$ transitions determined from x-ray fluorescence counting rates (circles) for ions generated with linearly polarized laser light with polarization parallel (top) and perpendicular (bottom) to the x-ray polarization. The data are the same as shown in panels (a) and (b) of Fig. 6. The major fitted components are Kr^+ $1s\rightarrow 4p_{1/2}$ (red curves), Kr^+ $1s\rightarrow 4p_{3/2}$ (blue curves), and Kr^{2+} (green curves). The tails of the higher Rydberg excitations (dashed curves) and continuum (dotted curves) of Kr^+ are also plotted. The solid black curves are the total fits.

Table I compares the experimentally and theoretically determined quantum state populations of strong-field-generated Kr^+. It is evident that the adiabatic strong-field ionization model we use reproduces the general trend displayed by the experimental state populations. The results of theory and experiment are in agreement that the majority of Kr^+ ions produced are in the $j=3/2$ state. Theory predicts a noticeable degree of alignment in this state: $\rho_{3/2,1/2}/\rho_{3/2,3/2}=17.8$. The experimental data also are consistent with Kr^+ alignment. However, the experimental ratio $\rho_{3/2,1/2}/\rho_{3/2,3/2}\approx 10$ is on the

TABLE I. Kr^+ quantum state populations $\rho_{j,|m|}$, following strong-field ionization of Kr, obtained from experiment and theory.

	$\rho_{j,\|m\|}(\%)$	
$\|j,m\rangle$	Experimental	Theoretical
$\|\frac{3}{2},\pm\frac{1}{2}\rangle$	59±6	71
$\|\frac{1}{2},\pm\frac{1}{2}\rangle$	35±4	25
$\|\frac{3}{2},\pm\frac{3}{2}\rangle$	6±6	4

low side of the theoretical ratio, which may be an indication of a partial failure of the adiabatic picture. The theoretical population of the $j=1/2$ state is also smaller than measured. We note that it requires the same number of photons (at 800 nm) to ionize either $4p_{3/2}$ or $4p_{1/2}$, and the experimental populations are consistent with the 2:1 statistical ratio. The adiabatic strong-field ionization model, which assumes an infinite wavelength, artificially suppresses the ionization of the more strongly bound $4p_{1/2}$ orbital. These deficiencies of the adiabatic strong-field ionization model were already anticipated in Ref. [11], but could not be demonstrated conclusively.

It is interesting to compare the present results with a recent study of strong-field laser ionization of Xe in which 55 eV high-order harmonic radiation was used as a $4d \rightarrow 5p$ probe of Xe^+ [15]. Similar theoretical calculations were employed in both cases to determine quantum state populations. In Xe, it takes one more 800-nm photon to ionize $5p_{1/2}$ than for $5p_{3/2}$. In that case, the adiabatic strong-field ionization model predicts the $j=1/2$ population quite accurately. However, the alignment of the $j=3/2$ state, as characterized by $\rho_{3/2,1/2}/\rho_{3/2,3/2}$, was overestimated by more than a factor of 4.

IV. CONCLUSION

A tunable, polarized, x-ray microprobe was used to record *K*-edge x-ray absorption spectra of laser-generated Kr^+ and Kr^{2+}. Prominent $1s \rightarrow 4p$ and $5p$ resonances are observed in both ions in agreement with calculated transition energies and probabilities [12]. The discrete transitions and shifted ionization thresholds distinguish the absorption spectra of the ions from that of neutral Kr. Alignment of Kr^+ $4p$ hole states is observed from the dependence of the $1s \rightarrow 4p$ cross section on the angle between the laser and x-ray polarization vectors [6]. The quantum state populations of Kr^+ $4p_{3/2}$ and $4p_{1/2}$ hole states were determined from fits to the $1s \rightarrow 4p_{3/2}$ and $4p_{1/2}$ cross sections. These data provide an experimental test of an adiabatic strong-field ionization theory that explicitly treats spin-orbit coupling [11]. The theoretical results are in general accord with the measurements, but limitations of the adiabatic model are indicated. This experiment and that of Ref. [15] demonstrate how spectroscopic probes of ions yield new insight into strong-field ionization.

The x-ray microprobe techniques have previously been applied to studies of the Coulomb expansion of the e^--Kr^+ plasma, dealignment of Kr^+, and observation of the effects of an external magnetic field [7]. Additional work on those topics is in progress. Future studies could include measurements of the polarization-dependent $1s \rightarrow 4p$ cross sections of Kr^{2+} for comparison with theories of strong-field double ionization. Measurements are needed to test calculated effects of laser dressing fields on the *K* edge absorption cross sections of Kr [40] and Ne [41]. The cross correlation technique, based on ultrafast atomic processes, could be used to characterize the ~ 1 ps x-ray pulses that are expected to be produced at the APS using RF deflecting cavities [42].

ACKNOWLEDGMENTS

We thank Lin Pan and Donald Beck for discussions of x-ray transition calculations and providing preliminary results. This work and use of the Advanced Photon Source was supported by the U.S. Department of Energy, Office of Science, Office of Basic Energy Sciences, under Contract No. DE-AC02-06CH11357.

[1] P. B. Corkum, Phys. Rev. Lett. **71**, 1994 (1993).
[2] L. F. DiMauro and P. Agostini, Adv. At. Mol. Phys. **35**, 79 (1995).
[3] E. A. Gibson, A. Paul, N. Wagner, R. Tobey, D. Gaudiosi, S. Backus, I. P. Christov, A. Aquila, E. M. Gullikson, D. T. Attwood, M. M. Murnane, and H. C. Kapteyn,Science **302**, 95 (2003).
[4] P. Agostini and L. F. DiMauro, Rep. Prog. Phys. **67**, 813 (2004).
[5] L. Young, R. W. Dunford, C. Hoehr, E. P. Kanter, B. Krässig, E. R. Peterson, S. H. Southworth, D. L. Ederer, J. Rudati, D. A. Arms, E. M. Dufresne, and E. C. Landahl, Radiat. Phys. Chem. **75**, 1799 (2006).
[6] L. Young, D. A. Arms, E. M. Dufresne, R. W. Dunford, D. L. Ederer, C. Höhr, E. P. Kanter, B. Krässig, E. C. Landahl, E. R. Peterson, J. Rudati, R. Santra, and S. H. Southworth, Phys. Rev. Lett. **97**, 083601 (2006).
[7] C. Höhr, E. R. Peterson, N. Rohringer, J. Rudati, D. A. Arms, E. M. Dufresne, R. W. Dunford, D. L. Ederer, E. P. Kanter, B. Krässig, E. C. Landahl, R. Santra, S. H. Southworth, and L. Young, Phys. Rev. A **75**, 011403(R) (2007).
[8] M. P. Hertlein, H. Adaniya, J. Amini, C. Bressler, B. Feinberg, M. Kaiser, N. Neumann, M. H. Prior, and A. Belkacem, Phys. Rev. A **73**, 062715 (2006).
[9] L. X. Chen, W. J. H. Jäger, G. Jennings, D. J. Gosztola, A. Munkholm, and J. P. Hessler, Science **292**, 262 (2001).
[10] V.-T. Pham, W. Gawelda, Y. Zaushitsyn, M. Kaiser, D. Grolimund, S. L. Johnson, R. Abela, C. Bressler, and M. Chergui, J. Am. Chem. Soc. **129**, 1530 (2007).
[11] R. Santra, R. W. Dunford, and L. Young, Phys. Rev. A **74**, 043403 (2006).
[12] L. Pan, D. R. Beck, and S. M. O'Malley, J. Phys. B **38**, 3721 (2005).
[13] R. F. Reilman and S. T. Manson, Phys. Rev. A **18**, 2124 (1978).
[14] M. Lu, G. Alna'washi, M. Habibi, M. F. Gharaibeh, R. A. Phaneuf, A. L. D. Kilcoyne, E. Levenson, A. S. Schlachter, C. Cisneros, and G. Hinojosa, Phys. Rev. A **74**, 062701 (2006).
[15] Z.-H. Loh, M. Khalil, R. E. Correa, R. Santra, C. Buth, and S. R. Leone, Phys. Rev. Lett. **98**, 143601 (2007).
[16] M. F. DeCamp, D. A. Reis, D. M. Fritz, P. H. Bucksbaum, E. M. Dufresne, and R. Clarke, J. Synchrotron Radiat. **12**, 177 (2005).
[17] H. Maeda, M. Dammasch, U. Eichmann, W. Sandner, A. Becker, and F. H. M. Faisal, Phys. Rev. A **62**, 035402 (2000).
[18] J. L. Chaloupka, R. Lafon, L. F. DiMauro, P. Agostini, and K.

C. Kulander, Opt. Express **8**, 352 (2001).
[19] P. J. Eng, M. Newville, M. L. Rivers, and S. R. Sutton, Proc. SPIE **3449**, 145 (1998).
[20] J. H. Hubbell, P. N. Trehan, N. Singh, B. Chand, D. Mehta, M. L. Garg, R. R. Garg, S. Singh, and S. Puri, J. Phys. Chem. Ref. Data **23**, 339 (1994).
[21] J. H. Scofield, Phys. Rev. **179**, 9 (1969).
[22] E. M. Dufresne, D. A. Arms, S. B. Dierker, R. Clarke, Y. Yacoby, J. Pitney, B. MacHarrie, and R. Pindak, Rev. Sci. Instrum. **73**, 1511 (2002).
[23] T. Matsushita and H. Hashizume, in *Handbook on Synchrotron Radiation*, edited by E. E. Koch (North Holland, Amsterdam, 1983), Vol. 1, pp. 261–314.
[24] E. M. Dufresne, J. A. Guzman, S. B. Dierker, R. Clarke, D. A. Arms, and D. A. Walko, in *SYNCHROTRON RADIATION INSTRUMENTATION: Eighth International Conference on Synchrotron Radiation Instrumentation*, AIP Conf. Proc. No. 705, edited by T. Warwick, J. Arthur, H. A. Padmore, and J. Stöhr (American Institute of Physics, Melville, NY, 2004), pp. 679–682.
[25] E. M. Dufresne, D. A. Arms, E. C. Landahl, and D. A. Walko, in *SYNCHROTRON RADIATION INSTRUMENTATION: Ninth International Conference on Synchrotron Radiation Instrumentation*, AIP Conf. Proc. No. 879, edited by J.-Y. Choi and S. Rah (American Institute of Physics, Melville, NY, 2007), pp. 950–953.
[26] M. O. Krause and J. H. Oliver, J. Phys. Chem. Ref. Data **8**, 329 (1979).
[27] M. Breinig, M. H. Chen, G. E. Ice, F. Parente, B. Crasemann, and G. S. Brown, Phys. Rev. A **22**, 520 (1980).
[28] R. D. Deslattes, E. G. Kessler, Jr., P. Indelicato, L. de Billy, E. Lindroth, and J. Anton, Rev. Mod. Phys. **75**, 35 (2003).
[29] O. Dragoun, A. Špalek, and F. J. Wuilleumier, Czech. J. Phys. **54**, 833 (2004).
[30] J. E. Sansonetti, W. C. Martin, and S. L. Young, *Handbook of Basic Atomic Spectroscopic Data* (National Institute of Standards and Technology, Gaithersburg, MD, 2005).
[31] *Handbook of Atomic, Molecular, and Optical Physics*, edited by G. W. F. Drake (Springer, New York, 2006).
[32] J. Berkowitz, *Photoabsorption, Photoionization, and Photoelectron Spectroscopy* (Academic Press, New York, 1979).
[33] S. J. Schaphorst, A. F. Kodre, J. Ruscheinski, B. Crasemann, T. Åberg, J. Tulkki, M. H. Chen, Y. Azuma, and G. S. Brown, Phys. Rev. A **47**, 1953 (1993).
[34] B. K. Agarwal, *X-Ray Spectroscopy* (Springer-Verlag, New York, 1991).
[35] A. R. Edmonds, *Angular Momentum in Quantum Mechanics* (Princeton University Press, Princeton, New Jersey, 1996).
[36] M. E. Rose, *Elementary Theory of Angular Momentum* (Dover, New York, 1995).
[37] U. V. Riss and H.-D. Meyer, J. Phys. B **26**, 4503 (1993).
[38] R. Santra and L. S. Cederbaum, Phys. Rep. **368**, 1 (2002).
[39] S. M. Hankin, D. M. Villeneuve, P. B. Corkum, and D. M. Rayner, Phys. Rev. A **64**, 013405 (2001).
[40] C. Buth and R. Santra, Phys. Rev. A **75**, 033412 (2007).
[41] C. Buth, R. Santra, and L. Young, Phys. Rev. Lett. **98**, 253001 (2007).
[42] M. Borland, Phys. Rev. ST Accel. Beams **8**, 074001 (2005).